Initial Analysis of Spectral Smile Calibration of Hyperspectral Imager Suite (HISUI) Using Atmospheric Absorption Bands

Satoru Yamamoto, Satoshi Tsuchida, Minoru Urai, Hiroki Mizuochi, Koki Iwao, and Akira Iwasaki

***Abstract*— This article reports on the initial analysis of spectral smile calibration of the Hyperspectral Imager Suite (HISUI) onboard the International Space Station, which has been continuously acquiring data since September 4, 2020. HISUI is an optical hyperspectral imager consisting of two subsystems: VNIR covering 400–980 nm at intervals of 10 nm and SWIR covering 895–2481 nm at 12.5-nm intervals. Based on the atmospheric correction for actual observation images, we assessed cross-track dependences of the wavelength deviation (spectral smile) and the full-width at half-maximum (FWHM) of the HISUI response function. We found that significant spectral smile was observed, with maximum variations of 1.8 nm in VNIR and 4.3–4.5 nm in SWIR. In addition, the cross-track variation of FWHM was observed with maximum variations of 5.0 nm for VNIR and 2.5–3.5 nm for SWIR. We used the results to model the smile functions to update a smile correction table in the internal calibration system of HISUI. Then, we evaluated how the smile functions reduce the spectral smile in the data acquired after the update on September 27, 2021. We confirmed that VNIR showed a nearly flat profile within 0.25 nm with a nearly constant FWHM. For SWIR, although a slight amount of spectral smile and a variation of FWHM were still observed partly due to wavelength dependence in the spectral smile, the spectral smile was reduced to less than ∼2.2 nm. This study demonstrated that wavelength calibration using actual observation images for ground surfaces is important for the characterization of hyperspectral sensors.**

***Index Terms*— Full-width at half-maximum (FWHM), Hyperspectral Imager Suite (HISUI), hyperspectral sensor, response function, spectral smile, wavelength calibration.**

I. Introduction

THE Hyperspectral Imager Suite (HISUI), developed by Japan's Ministry of Economy Trade and Industry (METI), is an optical sensor onboard the Japanese Experiment Module (JEM) of the International Space Station (ISS). HISUI is a push-broom-type sensor that acquires nadir hyperspectral images with two spectrometers (subsystems) collecting images at different wavelengths: VNIR covering 400–980 nm with a spectral resolution of 10 nm and SWIR covering 895–2481 nm with a spectral resolution of 12.5 nm. It was launched on December 6, 2019, and data acquisition has been continuously conducted since September 4, 2020, following initial checks of the sensor and adjustments to the data processing system on the ISS.

Hyperspectral data can be used to extract various information from discrete absorption and reflection features of a target surface or atmosphere. Thus, HISUI data are expected to be useful in various fields, such as natural resources, agriculture, forestry, environmental monitoring, and Earth science [1]. For such applications, both an accurate spectral calibration and a radiometric calibration are necessary for the reliability of the information extracted from hyperspectral data (see, e.g., [2]–[4]). In particular, for push-broom-type sensors, it is important to evaluate and calibrate the spectral smile, which is a phenomenon showing a cross-track dependence in a deviation from the original wavelength assignment caused by optical distortions incident on the detector array [5], [6]. Spectral smile has been reported and discussed for various hyperspectral sensors, such as Hyperion onboard the Earth Observing 1 (EO-1) [6]–[13], CHRIS onboard the European Space Agency Project for Onboard Autonomy (PROBA) [14], Compact Airborne Spectrographic Imager (CASI) [15], Portable Hyperspectral Imager for Low-Light Spectroscopy (PHILLS; airborne sensor) [9], CRISM onboard the Mars Reconnaissance Orbiter (MRO) [16], DLR Earth Sensing Imaging Spectrometer (DESIS) onboard the ISS [17], and PRecursore IperSpettrale della Missione Applicativa (PRISMA) [18]. Hence, it is important to evaluate spectral smile in the HISUI data and correct it appropriately.

HISUI has an internal system to correct spectral smile in the acquired data using a smile correction table that can be updated from the ground as needed [19]. The smile correction table was determined before launch based on the characteristics of spectral smile that were evaluated in a preflight test with the HISUI onboard calibration system (hereafter, onboard lamps), consisting of two halogen lamps and a filter wheel with wavelength calibration [20]. The evaluation of wavelength offsets using the filter wheel is included in the onboard calibration. No obvious spectral smile was reported in the analysis using the onboard calibration data, while it

Manuscript received 20 April 2022; revised 27 June 2022; accepted 8 July 2022. Date of publication 14 July 2022; date of current version 25 July 2022. This work was supported by the Ministry of Economy, Trade and Industry of Japan. *(Corresponding author: Satoru Yamamoto.)*

Satoru Yamamoto, Satoshi Tsuchida, Hiroki Mizuochi, and Koki Iwao are with the Geological Survey of Japan, National Institute of Advanced Industrial Science and Technology, Tsukuba 305-8567, Japan (e-mail: yamamoto.satoru@aist.go.jp).

Minoru Urai is with the Geological Survey of Japan, National Institute of Advanced Industrial Science and Technology, Tsukuba 305-8567, Japan, and also with Japan Space Systems, Tokyo 105-0011, Japan.

Akira Iwasaki is with the Graduate School of Engineering, The University of Tokyo, Tokyo 113-8656, Japan.

Digital Object Identifier 10.1109/TGRS.2022.3190486

was reported that wavelength offsets were 2.3 nm (VNIR) and 5.5 nm (SWIR) with respect to the preflight checks [21]. This indicates that while wavelength offsets exist, the smile correction table based on the preflight tests is still valid to correct the spectral smile in the HISUI data after launch.

Nevertheless, it is also important to evaluate spectral smile not only based on data from the onboard lamps but also based on actual observation images from the Earth's surface and atmosphere. This is because the path of the light from the lamps is slightly different from the path of light through the full optical system of the flight instrument to collect observational data. The difference in characteristics before and after launch may also be caused by gravity release. In other words, there is a possibility that the characteristics of spectral smile based on the onboard lamps is different from that of actual observational images, and in this case, the smile correction table determined based on the former does not enable sufficient spectral smile correction for actual observation images. Because the spectral smile in actual observation images was not examined in the preflight tests, the difference in the characteristics of spectral smile between the data from the onboard lamps and actual observation images is unknown.

Therefore, in this study, we evaluated spectral smile based on actual observation images using Earth's atmospheric molecular absorptions, which was partly based on the spectral calibration method for several hyperspectral sensors and field spectrometers [8], [13], [14], [22]. Atmospheric molecular absorptions in hyperspectral data allow us to evaluate spectral smile (e.g., [7]–[10], [15], [17], [18], [23]). The primary goal of this article is to evaluate spectral smile and examine smile functions used to update the smile correction table for the HISUI product.

In the remainder of this article, after giving a brief overview of HISUI in Section II, we describe how to evaluate spectral smile from actual observation images using the Earth's atmospheric molecular absorptions in Section III. We then evaluate spectral smile for VNIR and SWIR using this method in Section IV. In Section V, we examine the smile functions used to update the smile correction table based on the characteristics of the spectral smile and then describe how we verified that the updated table improves spectral smile correction in actual observational images.

II. Overview of HISUI

The general instrument characteristics of HISUI are summarized in Table I (more detailed information is given in [24]). HISUI consists of a reflecting telescope with a diameter of ~28 cm (focal length of 621.9 mm and f-number of 2.2), two gratings, and two 2-D detectors for VNIR and SWIR. The light passing through the reflecting telescope is imaged in double slits by an off-axis triple mirror. Then, light through the slits is detected in VNIR and SWIR. The VNIR detector is a 1024 × 256-pixel back-illuminated silicon complementary metal–oxide–semiconductor (CMOS) array detector with a pixel size of 30 μm × 30 μm. The SWIR detector is a 1000 × 256-pixel photovoltaic mercury cadmium telluride (PV-MCT) array detector with a pixel size of 30 μm × 30 μm and thermometrically controlled by a Stirling-type cryocooler. Each pixel in VNIR covers a wavelength range of 2.5 nm and each one in SWIR covers 6.25 nm. In ground-based calibration using tunable lasers and a Hg–Ar lamp, the spectral response function (SRF) of each spectral pixel is approximated by a Gaussian profile, and the full-width at half-maximum (FWHM) is reported to be about 2.9 nm for VNIR and 7.2 nm for SWIR [19]. In the internal data processing of HISUI, multiple pixels in the wavelength direction are binned as "one band," depending on the observation mode (see [19]). In a normal binning with no wavelength deviation, four pixels are binned as one band with a spectral resolution of 10 nm for VNIR, and two pixels are binned as one band with a spectral resolution of 12.5 nm for SWIR. Because the first four and the last two bands of VNIR and the first band of SWIR are out of specification, 58 out of 64 bands in the VNIR detector and 127 out of 128 bands in the SWIR detector are used. As a result, VNIR covers the wavelengths $\lambda = 400$–980 nm and SWIR covers $\lambda = 894.77$–2481.01 nm, where the coverages of the two detectors overlap in λ ranging from 894.77 to 980.00 nm. (Note that the two decimal digits in λ are a fraction of the total wavelength range divided by the number of bands.) The instantaneous field of view is 48.53 μrad, resulting in a spatial resolution of 20 m (cross-track direction) with a swath of 20 km in the case of a nominal altitude of the ISS of 410 km. The observation frequency is 4.36 ms, resulting in a spatial resolution in the along-track direction of 31 m for the nominal altitude of the ISS.

HISUI has three different observational modes: normal observation mode (hereafter, NR mode), high-resolution observation mode (HR mode), and Earth calibration observation mode (EA mode). Table II summarizes the major parameters for the three observation modes. The NR mode acquires data in 185 bands (total of 58 bands in VNIR and 127 bands in SWIR). The HR mode provides no binning data with spectral resolutions of 2.5 nm for VNIR and 6.25 nm for SWIR. In contrast, the available band range (hereafter, partition) for the HR mode is limited, where each partition has $1/4$ of the total number of bands for VNIR and $1/2$ of the total number of bands for SWIR (see Table II). This means that when we use the HR mode, we should choose one of four partitions for VNIR and one of two partitions for SWIR. The EA mode acquires no binning data with spectral resolutions of 2.5 nm for VNIR and 6.25 nm for SWIR without a limitation of the available band range. In contrast, the data acquisition interval is intermittent compared to the NR mode: $1/4$ in VNIR and $1/2$ in SWIR. For sensor calibration, arid desert areas that are relatively flat and have spectral uniformity were selected as target sites for the EA mode.

The data from the detectors are transmitted to the Hyper Electronics Unit (HELU) in HISUI after 12-b analog-to-digital conversion. To improve the data, the HELU conducts radiometric corrections of photoresponse nonuniformity, nonlinearity, and offsets, as well as the correction of the spectral smile [24]. The spectral smile is corrected with the binning process, where the contribution from each pixel is calculated using weighted coefficients. Since the details of the binning process are described in [19], only the main concepts

TABLE I
BASIC SPECIFICATIONS OF HISUI

	VNIR	SWIR
Detector	Si CMOS array detector	PV-MCT array detector
Wavelength range†	405.00–975.00 nm	901.02–2474.76 nm
Total number of bands	58	127
Wavelength resolution	10 nm	12.5 nm
Total number of samples	1024	1000
Nominal cross-track spatial resolution	20 m	
Nominal along-track spatial resolution	31 m	
Nominal observation swath	20 km	
Quantization	12 bits	
Signal-to-noise ratio	$\geq$ 450 at 620 nm	$\geq$ 300 at 2100 nm

†Center wavelength in the specification.

TABLE II
OBSERVATION MODES OF HISUI

	NR mode	HR mode	EA mode
Binning process	yes	no	no
Wavelength resolution for VNIR	10 nm	2.5 nm	2.5 nm
Wavelength resolution for SWIR	12.5 nm	6.25 nm	6.25 nm
Wavelength coverage for VNIR†	405.00–975.00 nm	Choose one of the following four partitions Partition 1: 405.00–522.50 nm Partition 2: 525.00–682.50 nm Partition 3: 685.00–842.50 nm Partition 4: 845.00–975.00 nm	405.00–975.00 nm
Wavelength coverage for SWIR†	901.02–2474.76 nm	Choose one of the following two partitions Partition 2: 901.02–1681.64 nm Partition 1: 1687.89–2474.76 nm	901.02–2474.76 nm

†Center wavelength in the specification.

are explained here. Let us consider the binning process for the band number i in VNIR. For simplicity of explanation, the description of a cross-track sample x_s is omitted below, although the actual equations are a function of x_s. The signal $\bar{S}(i)$ after binning is obtained as

$$\bar{S}(i) = \sum_{k=0}^{5} c_k(i) S(n(i)+k) \tag{1}$$

where $S(n(i)+k)$ is the original signal at spectral pixel of $n(i)+k$ and $n(i)$ is starting pixel for the band number i. The weighted coefficient $c_k(i)$ is normalized as

$$\sum_{k=0}^{5} c_k(i) = 1. \tag{2}$$

The values of $c_k(i)$ are determined to track the center wavelength so that the wavelength shift is corrected. The simplest example is a normal binning process with no wavelength deviation, in which the coefficients are $c_0(i) = c_5(i) = 0$ and $c_1(i) = c_2(i) = c_3(i) = c_4(i) = 1/4$. In contrast, for the case of wavelength deviation, signals from six spectral pixels are binned as one band, where the values of $c_k(i)$ are calculated such that the wavelength deviation is corrected. In other words, the spectral smile is corrected digitally at the same time as the binning process. For the SWIR, two spectral pixels are binned during the normal binning process, while signals from four spectral pixels are binned for the wavelength deviation (see [19] for more details). The data of $c_k(i)$ are compiled to a smile correction table uploaded from the ground [21]. The HELU performs the spectral smile correction according to the smile correction table.

The data after these corrections in the HELU are transmitted to the mission data processor, followed by recording to removable media on the ISS. The removable media are shipped from the ISS to the ground using a transport spaceship 3–4 times per year. In addition, a limited amount of data (up to ~10 GB per a day) from the removable media can be downloaded to the ground immediately after observation acquisition using the ISS communication system and the NASA Ku-band. In this study, we used the data downloaded with the ISS communication system.

The raw data (Level 0 data) in removable media brought down to the ground are processed to Level 1A data, which are then converted to Level 1R (L1R) data and Level 1G (L1G) data. A description of each data level is summarized in Table III. There are two data processing systems on the ground. One is the HISUI ground data system (GDS), which is operated and managed by Japan Space Systems [1], and the other is the calibration data archive system (CDAS) located at the Geological Survey of Japan, National Institute of Advanced Industrial Science and Technology [25]. The GDS generates HISUI Level 1 data (L1R and L1G data) for general users. Conversely, the CDAS is a ground data processing and archive system for calibration of the HISUI data. The data downloaded by the ISS communication system are also converted to L1R data in the CDAS. In addition, by applying the same radiometric corrections as those used in the HELU to the data (hereafter, EA data) of the EA mode on CDAS, we can also obtain L1R data from the EA data, which are in the same format as L1R data generated from the NR mode.

Preflight tests of the flight model (FM) were conducted to investigate the radiometric and spectral properties of

TABLE III
HISUI DATA PRODUCT

Name (abbreviation)	Description
Level 0 (L0)	Raw data not in image format
Level 1A (L1A)	Raw digital number data
Level 1R (L1R)	Radiance data
Level 1G (L1G)	Radiance data that are geometrically corrected

HISUI [20]. During these tests, the spectral smile characteristics were evaluated by the onboard lamps. In the preflight test in [20], VNIR and SWIR showed spectral smiles with a quadratic curve and maximum wavelength variations of 1.5 and 7 nm, respectively. The results of the preflight test were used to determine the smile correction table, which was then applied to the postlaunch data.

Finally, we should mention some of the observational limitations that are inherent to the ISS. Because the ISS is not in a sun-synchronous orbit: 1) the local time of observation is not constant; 2) the solar elevation varies largely with each observation; and 3) the HISUI observations are performed in both descending and ascending orbits. In addition, because the attitude of the ISS is always unstable, the target areas are not always observed as planned. Therefore, it is only by checking the data downloaded to the ground that we can determine whether the target area was actually observed. This situation limited the data availability for analysis in this study.

III. METHOD

In this study, we evaluated the wavelength deviation $\delta\lambda$ from its original wavelength assignment based on correction for atmospheric molecular absorptions using actual observation images. This analysis has the advantage of being able to evaluate the FWHM of the SRF of HISUI at the same time (see also [18], [26]). We then examined how $\delta\lambda$ depends on x_s in an image. In this section, we first describe atmospheric molecular absorptions and then explain how $\delta\lambda$ was determined from the correction of atmospheric molecular absorptions.

A. Atmospheric Molecular Absorptions

Fig. 1 shows major atmospheric absorption bands in several modeled radiances, which are calculated to model the upwelling radiance incident on HISUI using the radiative transfer code MODTRAN 6. In this figure, five modeled radiances are shown: one shows radiance assuming no atmospheric molecular absorptions by H_2O, O_2, CO_2, and CH_4 (a black curve), and the other four show radiance with atmospheric molecular absorptions by each of H_2O, O_2, CO_2, and CH_4, respectively. We can see that H_2O absorption bands (blue curve) are prominent, dominating all over the other molecular bands (green for O_2, red for CO_2, and pink for CH_4).

In our analysis, we did not use H_2O absorption bands to evaluate $\delta\lambda$ because the width of each absorption band for H_2O is too wide to determine the center wavelength with accuracy in the range of 1 nm or less. Another problem is that the amount of H_2O varies greatly with location and time and is also affected by water on the ground surface, resulting in large uncertainty in $\delta\lambda$. In contrast, absorption bands by O_2 and CO_2 are relatively narrow, allowing us to determine

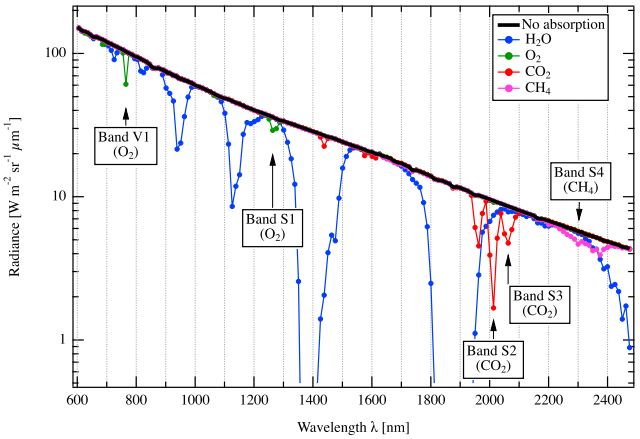

Fig. 1. Modeled radiance (black curve) assuming no atmospheric molecular absorptions by H_2O, O_2, CO_2, and CH_4, and four modeled radiances with each of the four atmospheric molecular absorptions by H_2O (blue curve), O_2 (green curve), CO_2 (red curve), and CH_4 (pink curve). All the modeled radiances were computed to model the upwelling radiance incident on HISUI using MODTRAN 6, where a Lambertian desert-barren surface was assumed for the BOA reflectance.

the center wavelength of these bands within 1 nm. As shown in Fig. 1, O_2 causes two absorption bands, where most of the λ values do not overlap with H_2O absorption bands: absorption bands centered at $\lambda = 765$ nm (hereafter, Band V1, although this is called oxygen A-band in general) and at $\lambda = 1260$ nm (hereafter, Band S1). In addition, we can also see three absorption bands due to CO_2 in $\lambda = 1900$–2100 nm, in which an absorption band centered at 2060 nm (hereafter, Band S3) does not overlap with those of H_2O and that at 2010 nm (hereafter, Band S2) has deep, narrow absorption and appears to be less affected by H_2O. Thus, we used Bands V1, S1, S2, and S3 for this analysis. In contrast, although most of λ for the CH_4 absorption band in $\lambda = 2200$–2400 nm does not overlap with the absorption bands of H_2O, the broad absorption band is not suitable for determining the central wavelength. Thus, we did not use the CH_4 absorption band to determine $\delta\lambda$. Table IV summarizes the absorption bands that were deemed suitable for the current analysis of spectral smile.

Note that the role of bottom-of-atmosphere (BOA) reflectance, especially absorption features from the ground surface, is important in the evaluation of $\delta\lambda$ based on the correction of atmospheric molecular absorption. This is because the absorption features in BOA reflectance can affect the shape of atmospheric molecular absorptions in the upwelling radiance incident on HISUI, which can lead to errors in the evaluation of $\delta\lambda$. Thus, the characteristics of the test sites used in this study should be spectrally uniform and have little variation in surface elevation. For this reason, arid desert areas by the EA mode were selected as the test sites in our analysis. In the modeled radiances in Fig. 1, a Lambertian desert-barren surface was assumed for the BOA reflectance.

B. Evaluation of the Spectral Smile by Atmospheric Correction

The analytical procedure to evaluate the spectral smile by atmospheric correction was given as follows. In this

TABLE IV
ATMOSPHERIC MOLECULAR BANDS USED IN THIS STUDY

Band name	Representative center wavelength [nm]	Molecular species	VNIR or SWIR
Band V1	765	O_2	VNIR
Band S1	1260	O_2	SWIR
Band S2	2010	CO_2	SWIR
Band S3	2060	CO_2	SWIR

TABLE V
WAVELENGTH RANGE FOR THE CALCULATION OF C_i

Band name	Beginning λ [nm]	End λ [nm]
Band V1	745.0	785.0
Band S1	1238.2	1288.2
Band S2	1987.6	2037.6
Band S3	2037.6	2087.6

analysis, we used the modeled radiance incident on HISUI from the target site, which was calculated using MODTRAN 6. MODTRAN calculations were performed using the U.S. Standard 1976 Atmospheric Profile, the desert aerosol model, and a Lambertian desert-barren surface type as representative parameter values. In addition, solar altitude, target latitude and longitude, ground height, and seasonal parameters were provided with values for each target and observation timing. These settings are a simple and efficient method for evaluating spectral smile for large numbers of pixels in a variety of HISUI scenes. Note that fine-tuning of MODTRAN parameters was not conducted for this analysis because the objective of this study was not to obtain accurate surface reflectance, but rather to estimate $\delta\lambda$ using atmospheric absorption bands.

Fig. 2(a) shows a comparison between the modeled and measured radiances for a desert region in Egypt, where the measured radiance was obtained as $x_s = 500$ and the modeled radiance was calculated using MODTRAN 6 with a Gaussian function of SRF (hereafter, the Gaussian model). We can see a concave feature around $\lambda = 765$ nm both for the measured and modeled radiances. We then calculated the ratio (hereafter, the radiance ratio) of the measured radiance to the modeled radiance, as shown in Fig. 2(b), where we can see a concave feature at $\lambda = 765$ nm (blue circles). The concave feature in the radiance ratio indicates that the shape of Band V1 in the modeled radiance is not consistent with that of the measured radiance. However, the concave feature can be dramatically reduced when a wavelength shift is adjusted for the measured radiance. For example, Fig. 2(b) also shows the radiance ratio for the case of the measured radiance shifted by $\omega = +0.4$ nm (red circles), where we obtained the shifted data using the cubic spline interpolation (see, e.g., [27]). We see that the radiance ratio around $\lambda = 745$–785 nm with $\omega = +0.4$ nm becomes nearly flat compared to that with $\omega = 0.0$ nm. Thus, when we find a nearly flat radiance ratio by searching for the best solution of ω, we can estimate that the amount of the wavelength shift $\delta\lambda$ is $\delta\lambda = -\omega$.

The best solution of ω was determined from the following procedure. We first obtained the shifted data of the measured radiance with a given ω and then calculated the radiance ratio R_i for the shifted data, where the subscript i indicates the band number. We then obtained a continuum C_i by linear fitting to the data point at $\lambda = 745$–785 nm of R_i. The root-mean-square (rms) value χ of the difference between R_i and C_i was calculated as

$$\chi = \sqrt{\sum_{i=i_{\min}}^{i_{\max}} (R_i - C_i)^2} \tag{3}$$

where $i_{\min}$ and $i_{\max}$ are band numbers that correspond to $\lambda = 745$ and 785 nm, respectively. Wavelength ranges that correspond to $i_{\min}$ and $i_{\max}$ for Bands V1, S1, S2, and S3 are listed in Table V. While searching for ω in increments of 0.1 nm, we attempted to find the condition under which χ has the minimum value. Fig. 2(c) shows an example how χ varies with ω for the data of Fig. 2(a). We can see that the minimum χ is located at $\omega = +0.4$ nm, indicating $\delta\lambda = -0.4$ nm at $x_s = 500$.

The reason why the radiance ratio is not exactly unity in Fig. 2(b) is that the reflectance model used in the calculation by MODTRAN does not perfectly represent the ground surface. However, as mentioned above, the objective of this study was not to obtain accurate surface reflectance by accounting for the atmospheric correction, but rather to evaluate efficiently the spectral smile for the HISUI data. Therefore, no further tuning to obtain a radiance ratio of 1 was performed in this study.

C. Spectral Response Function

To determine ω from the atmospheric correction, the evaluation of the SRF is also important [2]. The SRF model for HISUI was determined based on the preflight tests and compiled in the radiometric database (RD) [25] (hereafter, the RD model) in the CDAS. However, we found that the RD model does not provide an adequate optimal solution for ω. Fig. 3(a) shows the radiance ratios for various ω values when the RD model was used. We can see that there are dip and spike features for $\lambda = 745$–775 nm, indicating inappropriate atmospheric correction for Band V1. We also tried to find a better solution of ω for a wider range of ω ranging from -3.0 to $+3.0$ nm but could not find an ω value that would reduce the dip and spike features for $\lambda = 745$–775 nm. Moreover, we tried adjusting the oxygen partial pressure with changes in the elevation and seasonal atmospheric model, but in none of the cases could we reduce the dip and spike features. Fig. 3(b) shows the relation between χ and ω when the RD model was used. We can see the lowest value of $\chi \sim 0.074$ at $\omega = 0.0$–0.1 nm, which is much larger than $\chi \sim 0.009$ for the Gaussian model shown in Fig. 2(c). However, as shown in Fig. 2(b), the Gaussian model can obtain a nearly flat radiance ratio for $\lambda = 745$–775 nm without additional adjustments except for the tuning of ω.

Therefore, the Gaussian model can provide a more appropriate optimal solution for ω than can the RD model. In this case, the FWHM W_{FM} of the Gaussian model is also an important parameter. This means that we need to search for the best solution for both ω and W_{FM} that minimizes χ. Since we do not know the explicit expression of χ, we cannot analytically

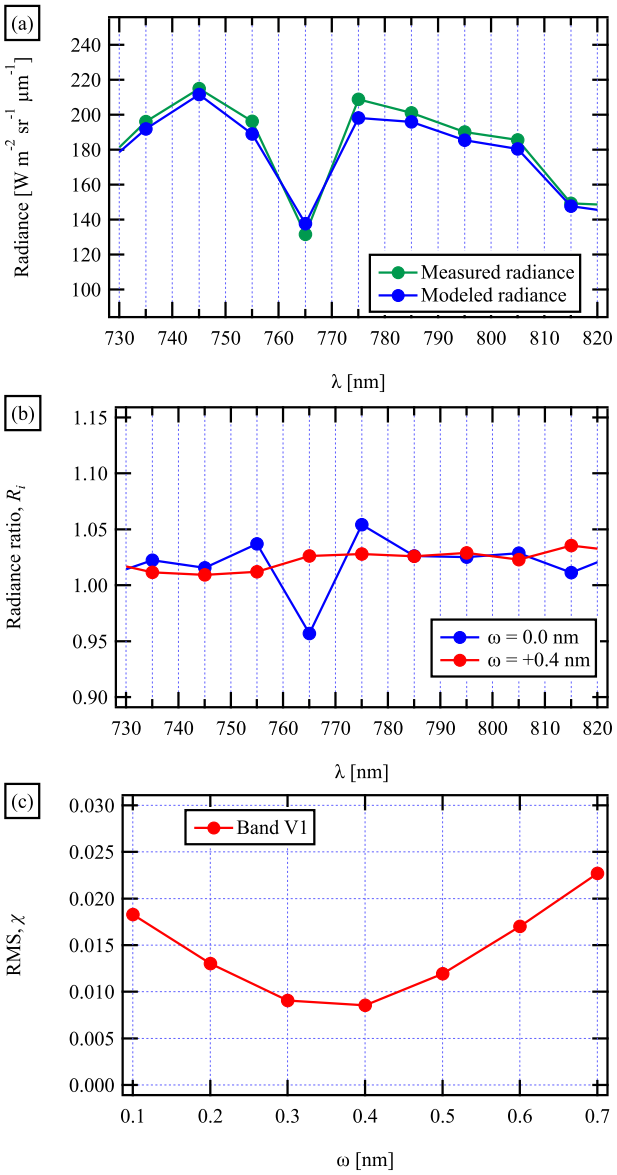

Fig. 2. (a) Radiance measured by HISUI for a desert region in Egypt, data ID 210603 (green circles) ($x_s = 500$ in the image) and modeled radiance convolved with the Gaussian model (blue circles). (b) Radiance ratio (blue circles) for the case of (a) without adjusting the wavelength shift ($\omega = 0.0$ nm). For comparison, the radiance ratio with $\omega = +0.4$ nm is also plotted (red circles). (c) RMS value χ for Band V1 plotted against ω.

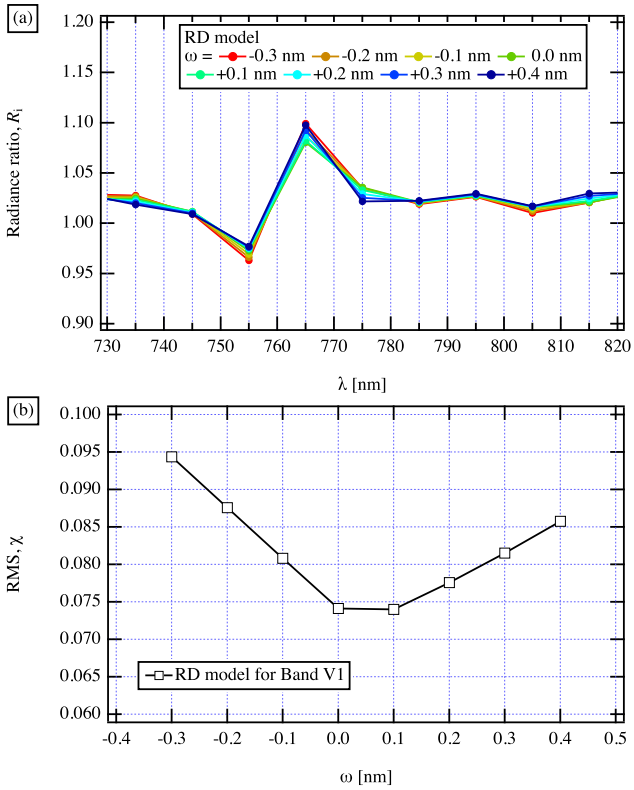

Fig. 3. (a) Radiance ratios for the same target area as that in Fig. 2 for various ω values, which were calculated using the RD model rather than the Gaussian model. Dip and spike features can be seen for $\lambda = 745$–775 nm. (b) RMS χ plotted against ω for (a).

obtain the optimal solution for both ω and W_{FM}. Thus, in this study, the optimal solution is obtained by performing grid search for the parameter space of ω and W_{FM}, where grid search is a tuning technique that attempts to compute the optimum values for various parameters. We calculated χ for various values of ω and W_{FM}, where the range of search for ω was set to be -4.0 to 7.0 nm with an increment of 0.1 nm and the range of search for W_{FM} was set to be 4.0 nm to 24.0 nm with an increment of 0.25 nm. The combination of ω and W_{FM}, which minimizes χ among all calculations, was then selected as the optimal solution. Fig. 4(a) shows how χ varies with W_{FM} and ω. It is seen that χ for each W_{FM} shows a quadratic curve with ω. Note that all the results of the Gaussian model shown in Fig. 4(a) have minimum values of $\chi <\sim 0.03$ lower than those of the RD model ($\chi \sim 0.075$). It is also seen that χ with $W_{\mathrm{FM}} = 7.75$ nm has the lowest value among all the results shown here. Fig. 4(b) shows the radiance ratios for various ω values for the case of $W_{\mathrm{FM}} = 7.75$ nm. While we can see that the radiance ratio around $\lambda = 765$–775 nm varies with ω, the radiance ratio with $\omega = 0.5$ nm becomes nearly flat. In Fig. 4(c), we also compare the radiance ratio for the best solution of the Gaussian model ($\omega = 0.5$ nm) with that of the RD model ($\omega = 0.1$ nm), where it is clear that the former has a nearly flat radiance ratio compared with the latter. Therefore, we concluded that we should use the Gaussian model rather than the RD model.

D. Data

In this study, we mainly used the EA data because the target areas for the EA data are desert areas, which are expected to be bright, spectrally uniform and with little variation in surface elevation. Another reason is that the EA data are being downloaded to the ground on a priority basis using the ISS communication system. If the NR mode data were used for analysis, it would have been necessary to wait for the data media to return to Earth on a transport spaceship, except for special priority downloaded data. However, because HISUI does not have a pointing system, the opportunity to acquire the EA data in desert areas is limited to several times a year. So far, four sets of EA data suitable for this analysis have been obtained. Table VI summarizes the observation sites and dates

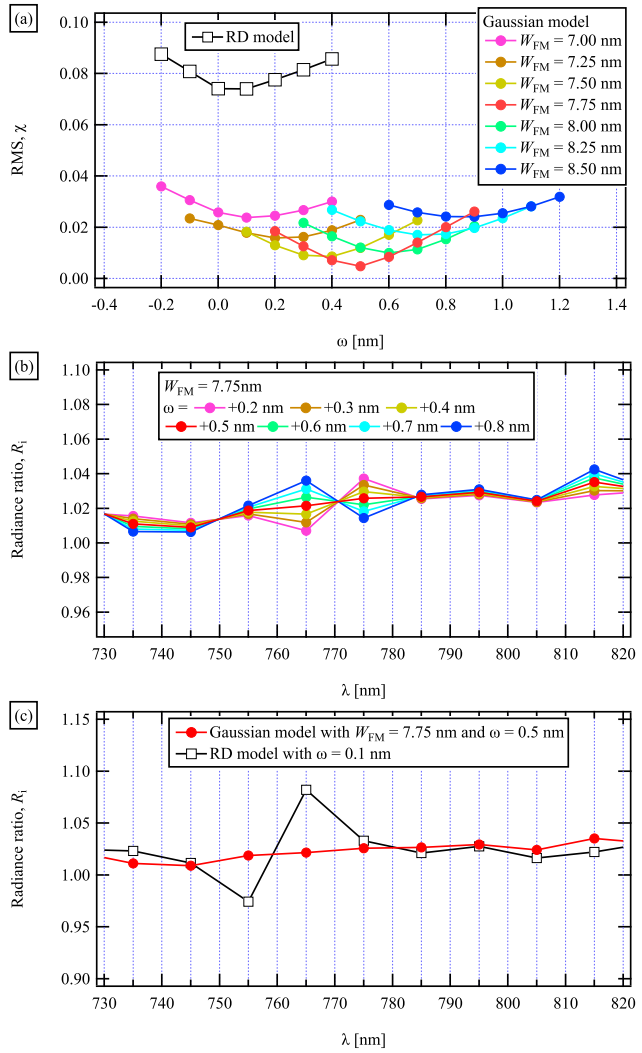

Fig. 4. (a) χ plotted against ω for various W_{FM}'s for the Gaussian model (data ID 210603 and $x_s = 350$). We calculated χ for various values of ω with an increment of 0.1 nm and W_{FM} with an increment of 0.25 nm to find the combination of ω and W_{FM} that minimizes χ among all calculations. In this example, χ with $W_{FM} = 7.75$ nm and $\omega = 0.5$ nm has the lowest value among all the results. For comparison, χ for the RD model is plotted (open rectangles). (b) Radiance ratios for the Gaussian model with $W_{FM} = 7.75$ nm for various ω values plotted against λ. (c) Radiance ratio at the best solution with $W_{FM} = 7.75$ nm and $\omega = 0.5$ nm (red circles) plotted against λ. For comparison, the radiance ratio with $\omega = 0.1$ nm for the RD model is plotted (open rectangles).

for the EA data. Unfortunately, VNIR data for IDs 210607, 210611, and 210618 are not available due to data loss, which may have occurred during the downlink process. Therefore, only the SWIR data were analyzed for these three datasets. In contrast, both VNIR and SWIR data were usable for ID 210603.

In addition, we also analyzed two NR mode datasets (IDs 211002 and 211025) for relatively homogeneous, flat barren regions, which were downloaded using the ISS communication system for the purpose of assessing the performance after an update of the smile correction table, as described in Section V-C. There are also downloaded NR data that were measured from a desert area (ID 210101), but many areas of the image were covered by clouds. Thus, some cloudless

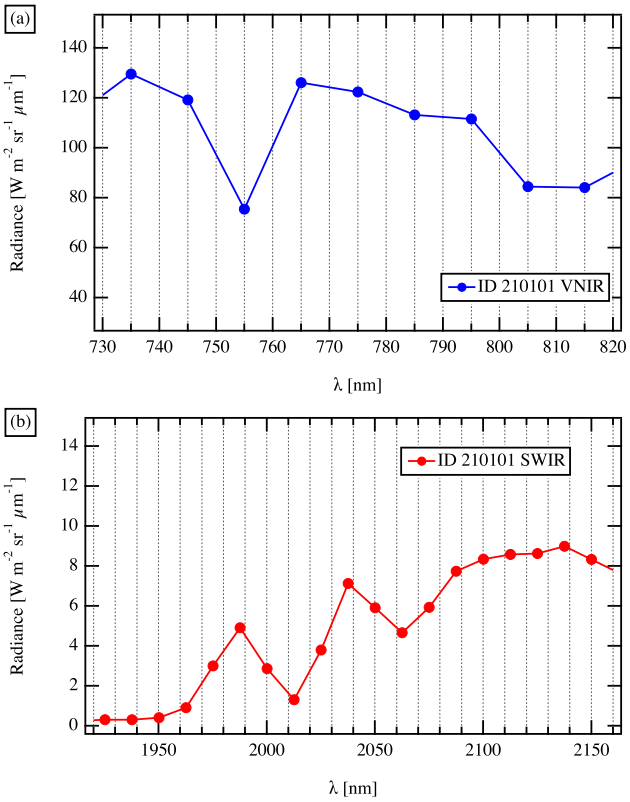

Fig. 5. (a) Measured radiance of the NR mode data for ID 210101 VNIR. A dip feature is seen at $\lambda = 755$ nm but not at $\lambda = 765$ nm, as expected for Band V1. (b) Measured radiance of the NR mode data for ID 210101 SWIR. Two absorption bands centered around $\lambda = 2010$ and 2060 nm correspond to the expected ones of Bands S2 and S3, respectively.

areas in this data were used to confirm the band allocation, as described in Section IV-A.

IV. Results

A. Band Shift Phenomenon in VNIR

Before evaluating the spectral smile, we first checked whether the band allocation matched the expected wavelengths in the NR mode data using Bands V1, S1, S2, and S3. Fig. 5(a) shows the measured radiance of the NR mode data for VNIR, which was measured in a desert area (ID 210101). We can see that a dip feature is observed at 755 nm, exactly one band off from 765 nm, as expected for Band V1. Because the dip feature at 755 nm is seen everywhere in a scene regardless of the sample and line, we conclude that the VNIR data of the NR mode are always shifted by one band (10 nm) to the shorter wavelength (hereafter, we call this the band shift phenomenon). In contrast, we also found that the L1R data derived from the EA data do not show the band shift phenomenon, as shown in Fig. 2. Thus, the band shift phenomenon is probably due to a misallocation of the center wavelengths in the band registration in the HISUI binning process [19], rather than a problem with the optical instrument. The HISUI project has already corrected the assignment for VNIR in the ground L0 process. Hence, this problem does not exist in the HISUI public data.

Fig. 5(b) shows the measured radiance of the NR mode data for SWIR. We can see that there are two absorption bands

TABLE VI
CONDITIONS OF TARGET AREAS

Observation ID	Date	Mode	Target area	Latitude and longitude†	Elevation [km]	Solar elevation angle [deg]	Data availability
210101	January 1, 2021	NR	Desert (Saudi Arabia)	25.522°N, 46.607°E	0.9	30	VNIR & SWIR
210603	June 3, 2021	EA	Desert (Egypt)	21.893°N, 28.451°E	0.3	87	VNIR & SWIR
210607	June 7, 2021	EA	Desert (Egypt)	21.793°N, 28.348°E	0.25	66	SWIR
210611	June 11, 2021	EA	Desert (Egypt)	21.853°N, 28.370°E	0.25	44	SWIR
210618	June 18, 2021	EA	Desert (Libya)	24.313°N, 13.448°E	0.6	47	SWIR
211002	October 2, 2021	NR	Barren (Turkmenistan)	37.879°N, 54.065°E	< 0.02	44	VNIR & SWIR
211025	October 25, 2021	NR	Barren (U.S.)	36.220°N, 110.242°W	1.7	41	VNIR & SWIR

†Center latitude and longitude at the representative center point calculated by the HISUI scheduler using the ISS orbit prediction data.

centered around $\lambda = 2010$ and 2060 nm, which correspond to the expected ones of Bands S2 and S3, respectively. Thus, we confirmed that no band shift phenomenon was observed in SWIR, indicating that the appropriate band allocations were made in SWIR.

B. Spectral Smile and FWHM: VNIR

We next evaluated the spectral smile for VNIR based on the EA data. Fig. 6 shows a color composite image for the ID 210603 VNIR, where red, green, and blue are assigned to the bands of $\lambda = 725$, 515, and 665 nm, respectively. We selected five lines (marked "Line A"–"Line E"), all of which are considered to be spectrally homogeneous and with little variation in surface elevation. Then, the optimal solutions of ω (and $\delta\lambda$) and W_{FM} were obtained at 20-sample intervals ("+" symbols) in each line using the method described above. In Fig. 7(a), $\delta\lambda$ for Band V1 is plotted against x_{s}. We can see that all the overall trends of $\delta\lambda$ show a quadratic curve, where $\delta\lambda$ around $x_{\mathrm{s}} = 400$–600 is approximately -0.4 ± 0.1 nm and $\delta\lambda$ at both ends of x_{s} decreases down to -1.7 nm (the left end) or -2.2 nm (the right end). An average of the five different lines is also plotted as a red curve, where we see that the typical difference between the average and each line is less than $\sim$0.1 nm. From the average value, we estimate that the maximum difference in $\delta\lambda$ between the center and ends of x_{s} is $\Delta\lambda_{\max} \sim 1.8$ nm.

In Fig. 7(b), W_{FM} for Band V1 is plotted against x_{s}. Similar to $\delta\lambda$, the overall trends of W_{FM} show a quadratic curve with the lowest value of $W_{\mathrm{FM}} \sim 6.75$ nm around $x_{\mathrm{s}} = 500$ and W_{FM} at both ends of x_{s} increases up to $W_{\mathrm{FM}} = 11.0$ nm (the left end) or 12.0 nm (the right end). The average of the five different lines is also plotted as a red curve, where the typical difference between the average and each line is less than $\sim$0.2 nm. From the average value, the maximum difference in W_{FM} between the center and ends of x_{s} is $\sim$5 nm. Thus, both $\delta\lambda$ and W_{FM} of VNIR show significant cross-track dependence.

The FWHM of the data after the binning process depends on $c_k(i)$ in (1), which is determined based on spectral smile characteristics. This is why, as with the smile characteristic, W_{FM} shows cross-track dependence. Thus, if the spectral smile is appropriately corrected, the cross-track dependence of W_{FM} would be corrected at the same time, as shown in Section V-C.

Note that jagged patterns are common to all five lines in both $\delta\lambda$ and W_{FM} in Fig. 7. For example, we can see the jagged pattern that is common to the five lines at $x_{\mathrm{s}} = 140$ [black arrows in Fig. 7(a) and (b)], showing similar values of $\delta\lambda = -0.3$ nm and $W_{\mathrm{FM}} = 8$ nm, respectively. We can also see that such jagged patterns are common to the five lines at other x_{s} values (e.g., red arrows at $x_{\mathrm{s}} = 60$ and $x_{\mathrm{s}} = 920$). This suggests that the jagged patterns are not due to spectral variation in the surface properties or atmospheric variation, but rather to subtle imperfections in the relative radiometric calibration which also affect the spectral characteristics.

Fig. 6. Color composite image for the VNIR data for ID 210603, where red, green, and blue are assigned to the bands of 725, 515, and 665 nm, respectively. Black "+" symbols indicate the position for determining $\delta\lambda$ and W_{FM}.

Since VNIR uses a back-illuminated Si-CMOS detector, there is the possibility that fringing (etaloning) affects the evaluation of spectral smile using Band V1 (see, e.g., [17]). In this case, interference patterns may appear in the spectral smile data due to coherent light reflected at the front and back of the detector, as shown in the DESIS analysis in [17]. However, since no data, including preflight test data, are

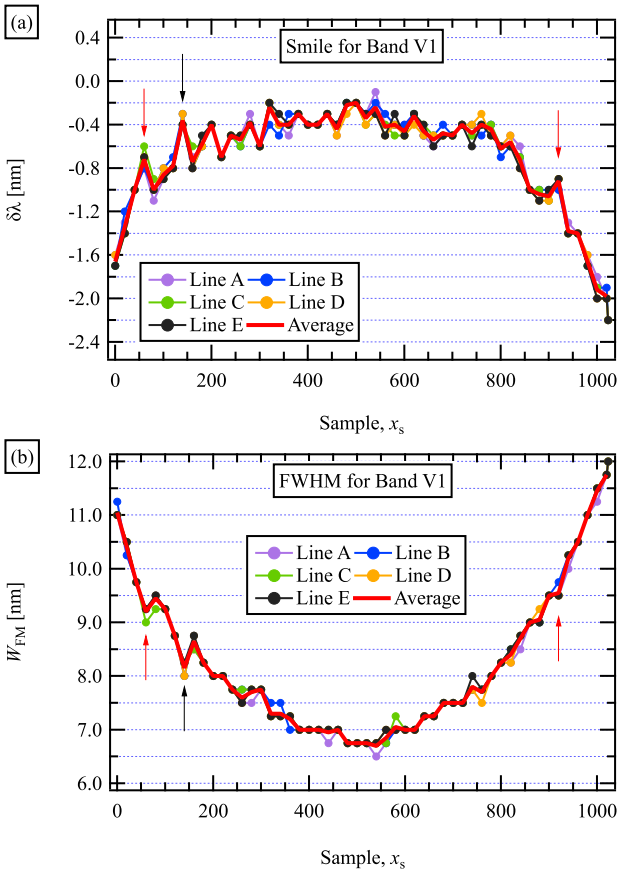

Fig. 7. Values of (a) $\delta\lambda$ and (b) W_{FM} for Band V1 (O_2 absorption band at $\lambda = 765$ nm) for ID 210603 plotted against x_s. Red curves indicate the average of the five lines A, B, C, D, and E in Fig. 6. Black arrows denote an inherent jagged pattern at $x_s = 140$, and red arrows denote inherent jagged patterns at $x_s = 60$ and 920.

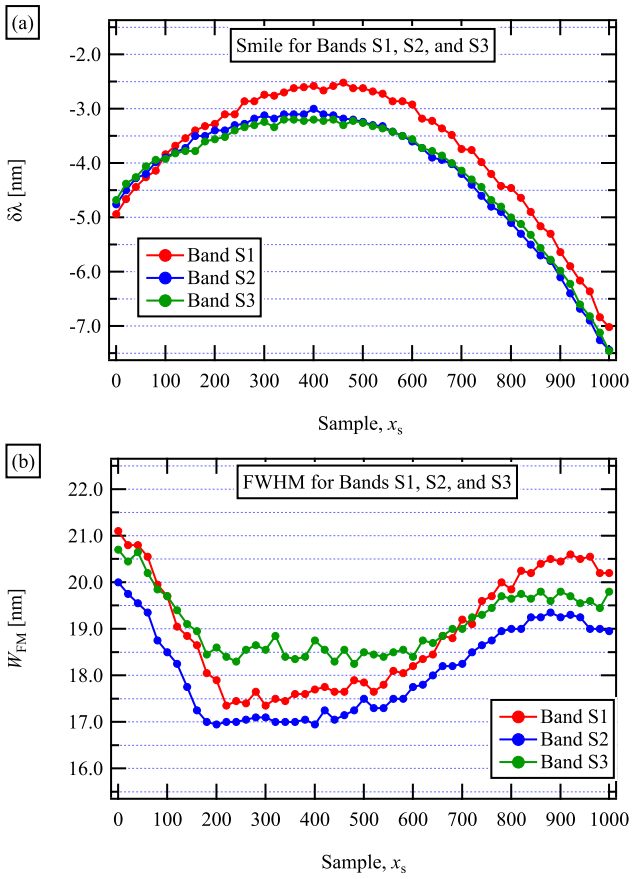

Fig. 8. (a) $\delta\lambda$ and (b) W_{FM} for SWIR for Bands S1 (O_2 1260-nm absorption band), S2 (CO_2 2010 nm-absorption band), and S3 (CO_2 2060-nm absorption band) of ID 210603.

available to confirm the appearance of interference patterns in spectral smile data, we cannot say whether etaloning affects the estimation of spectral smile.

C. Spectral Smile and FWHM: SWIR

We next determined $\delta\lambda$ and W_{FM} for the ID 210603 SWIR. Because we found that the typical difference between the average and each individual line result is less than ~0.1 nm for Bands S1, S2, and S3, only the average values of the five lines are shown in the following. In Fig. 8(a), the average values of $\delta\lambda$ of the five lines for Bands S1, S2, and S3 are plotted against x_s. It is seen that all the results show a quadratic curve, where the values of $\delta\lambda$ around $x_s = 400$–450 are approximately −2.5 nm (Band S1) and approximately −3.2 nm (Bands S2 and S3), and decrease down to −4.7 to −5.0 nm (the left end) and −7.0 to −7.5 nm (the right end). It is also seen that the spectral smile of SWIR has an asymmetric distribution, where $\delta\lambda$ on the right side is lower than that on the left side for all bands. From these results, we estimated that $\Delta\lambda_{max} = 4.5$ nm (Band S1), 4.4 nm (Band S2), and 4.3 nm (Band S3).

In Fig. 8(b), the average of W_{FM} for Bands S1, S2, and S3 is plotted against x_s. We can see that the results of W_{FM} exhibit the cross-track dependence. However, the overall trends are irregular, asymmetric curves, which are different from those for VNIR. For example, for the case of Band S1, while the center region of $x_s = 200$–500 has a nearly constant of $W_{FM} =$ 17.5–18.0 nm, W_{FM} at the left end increases up to ~21 nm and W_{FM} at the right side increases to 20.5 nm but drops slightly at the end. As a result, the maximum variation in W_{FM} is 3.5 nm for Band S1. The results for Bands S2 and S3 also show irregular curves similar to that for Band S1, with maximum variations of 3.0 nm (Band S2) and 2.5 nm (Band S3). Therefore, both $\delta\lambda$ and W_{FM} exhibit an asymmetric cross-track dependence.

For comparison, we determined $\delta\lambda$ and W_{FM} for SWIR of IDs 210607, 210611, and 210618, where the five lines selected in the analysis are shown in Fig. 9(a)–(c). The left column of Fig. 10 summarizes the results of $\delta\lambda$ for various ID data, where the average values of $\delta\lambda$ for Bands S1, S2, and S3 are plotted against x_s. We can see that the overall trends of $\delta\lambda$ show a quadratic curve and that there is no significant difference among the various datasets, with a maximum difference of <0.1–0.2 nm. In addition, the right column in Fig. 10 summarizes W_{FM} for Bands S1, S2, and S3 with respect to x_s. Although there is a small difference of <0.6 nm among the various datasets, the overall trends of the cross-track dependence are similar to each other. These results indicate that there is no significant scene-to-scene or short-term diurnal variations in $\delta\lambda$ and W_{FM}. Note that it has

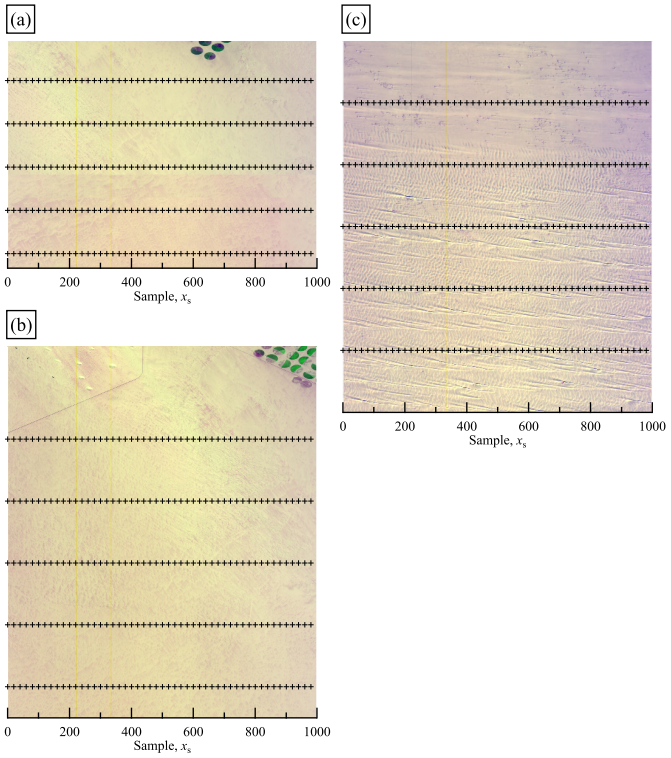

Fig. 9. Color composite images for the SWIR data of (a) ID 210607, (b) ID 210611, and (c) ID 210618, where red, green, and blue are assigned to the bands of 1638, 1501, and 1013 nm, respectively. Black "+" symbols indicate the positions used to determine $\delta\lambda$ and W_{FM}. The reason why ID 210607 produces a shorter image than the others in the along-track direction is due to a partial loss of data, which may have occurred during the data transfer process.

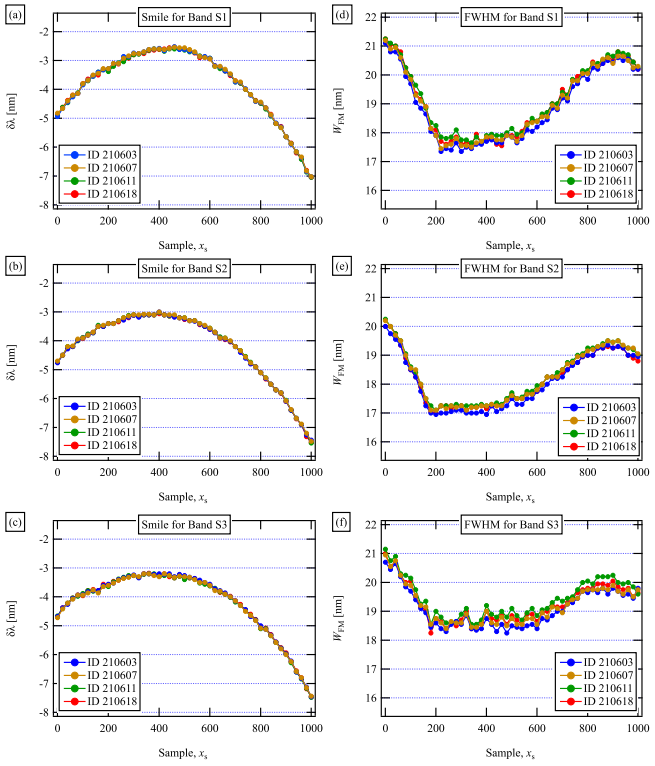

Fig. 10. $\delta\lambda$ for Bands (a) S1, (b) S2, and (c) S3 for IDs 210603, 210607, 210611, and 210618. W_{FM} for Bands (d) S1, (e) S2, and (f) S3 for IDs 210603, 210607, 210611, and 210618.

been reported that smile characteristics in the Hyperion data vary from scene to scene (see [10]).

D. Wavelength Dependence of Spectral Smile

While the wavelength dependence of $\Delta\lambda_{\max}$ for VNIR cannot be discussed here because of its limitation to single-band data (only Band V1), we can examine the wavelength dependence of $\Delta\lambda_{\max}$ for SWIR. In Fig. 11(a), $\Delta\lambda_{\max}$ is plotted against the center wavelength of each band. We can see that $\Delta\lambda_{\max}$ at $\lambda = 2010$ and 2060 nm (Bands S2 and S3, respectively) seems to be 0.1–0.2 nm lower than at $\lambda = 1260$ nm (Band S1), although the difference between S1 and S2 is within the error bar. It is also seen that $\Delta\lambda_{\max}$ at $\lambda = 2060$ nm seems to be lower than that at $\lambda = 2010$ nm, although its difference is within the error bar. Therefore, we found a slight wavelength dependence in $\Delta\lambda_{\max}$, but the maximum difference between Bands S1 and S3 is within 0.2 nm. Note that ground-based calibration using three solid-state lasers ($\lambda = 1200$, 1650, and 1775 nm) also showed a slight wavelength dependence in magnitude and shape of the spectral smile, with a typical difference among three wavelengths being about a few tenths of a nanometer [19].

In Fig. 11(b), the difference in $\Delta\lambda_{\max}$ between the left and right ends of x_s is plotted against the center wavelength, which may indicate the degree of the asymmetrical distribution in the spectral smile. It can be seen that the difference between the left and right ends increases with increasing λ, and the difference between Band S1 and Bands S2/S3 is ~0.6 nm. This suggests that the asymmetry in the spectral smile is larger for longer wavelengths. In fact, Fig. 10(a) and (c) shows that the peak position of $\delta\lambda$ of Band S3 is located around $x_s \sim 400$, which is slightly to the left of the peak position of Band S1 at $x_s \sim 450$. This may indicate that the degree of the distortion of light from the slit at the focal plane varies with λ.

In summary, we found that there is a slight wavelength dependence in the spectral smile, but the maximum wavelength dependence of $\Delta\lambda_{\max}$ is within 0.2 nm. In contrast, the maximum difference of $\Delta\lambda_{\max}$ between the left and right ends is up to ~0.6 nm between Bands S1 and S2/S3.

V. Discussion

Based on the actual observation images for ground surfaces, we found a significant spectral smile with maximum variations of 1.8 nm in VNIR and 4.3–4.5 nm in SWIR. However, the data from the onboard lamps did not show such a spectral smile [21]. This difference can be attributed to the fact that the path of the light from the onboard lamps is not exactly the same as the path of light in the full optical system of the instrument that obtains observational data. The problem is that the smile correction table determined based on the preflight data using the onboard lamps causes "false spectral smile" in the actual observation images. Therefore, we need to update the smile correction table based on the characteristics of spectral smile observed in the actual observation images.

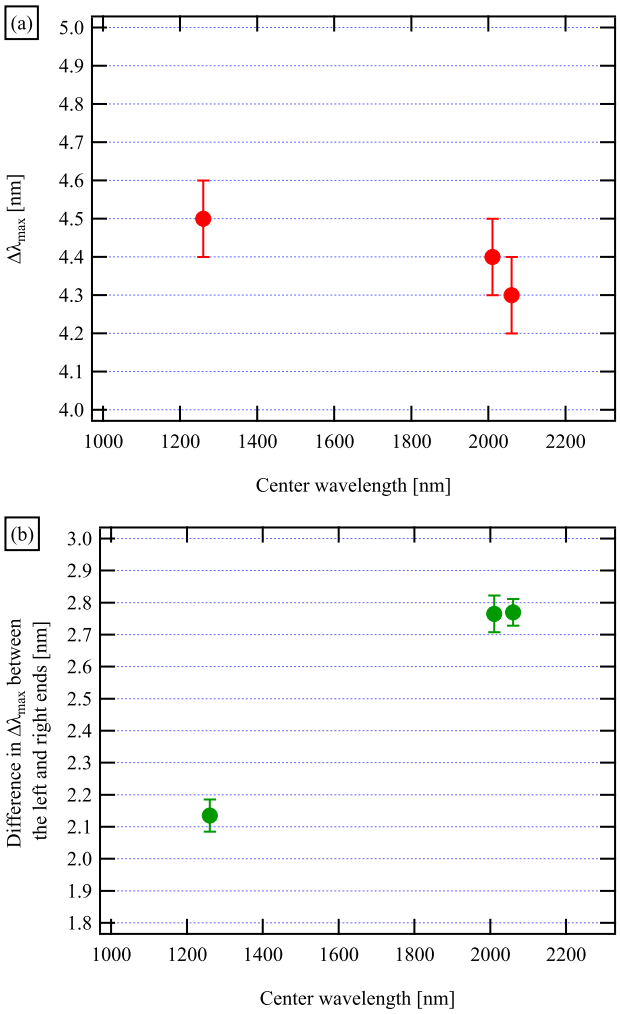

Fig. 11. (a) Relation between $\Delta\lambda_{max}$ and the center wavelength of each band. (b) Difference in $\Delta\lambda_{max}$ between the left and right ends of the sample plotted against the center wavelength.

In the HISUI project, the smile correction table was updated on September 27, 2021, following the report of the above spectral smile. In the following, we describe the smile function used to update the smile correction table and then describe how we verified that the updated table reduces spectral smile in the actual observation images.

A. Updating the Smile Correction Table

For the smile function $\delta\lambda_M$, we assumed a quadratic curve as

$$\delta\lambda_M = a_0 + a_1 x_s + a_2 x_s^2 \tag{4}$$

where $\delta\lambda_M$ is measured in nanometers and a_0, a_1, and a_2 are the coefficients obtained from a quadratic curve fitting using the results of $\delta\lambda$ for ID 210603. However, contrary to the procedure used in this article, the determination of the coefficients in the HISUI project was based on the data from every 50 samples from three lines. This is because the HISUI project had to take urgent action after the spectral smile was found in the actual observation images, and time was not available for further analysis. In addition, it was assumed that the amount of spectral smile is independent of λ for SWIR, and a_0, a_1, and a_2 were determined from the average values of $\delta\lambda$ for Bands S1 and S3.

From a least-square fitting with (4), the smile function for VNIR was determined as

$$\delta\lambda_M = -1.48 + 5.36 \times 10^{-3} x_s - 5.47 \times 10^{-6} x_s^2. \tag{5}$$

For SWIR

$$\delta\lambda_M = -4.73 + 9.59 \times 10^{-3} x_s - 1.20 \times 10^{-5} x_s^2. \tag{6}$$

Table VII summarizes the values of coefficients a_0, a_1, and a_2 determined for VNIR and SWIR. The HISUI data acquired after September 29, 2021, which corresponds to the first date after the update of the smile correction table, were corrected with the coefficients in Table VII.

B. Difference in the Smile Function

To evaluate the difference in the smile function due to the limited data from every 50 samples from three lines and the assumption of λ independence, we compared the data of $\delta\lambda$ in Figs. 7 and 10 with the results derived from the smile function of (5) and (6). Fig. 12(a) shows the difference between $\delta\lambda$ in Fig. 7(a) and the smile function of Eq. (5) for VNIR. We can see that there is a slight variation with x_s in the difference in $\delta\lambda$, where the center region around $x_s = 200$ to $\sim$700 has a negative value, but it is positive near both ends around $x_s = 50$–200 and $x_s = 700$–900. We can also estimate that the typical difference is less than $\sim$0.2 nm with a maximum difference of $\sim$0.4 nm.

Fig. 12(b)–(d) shows the differences in $\delta\lambda$ between Fig. 10(a)–(c) and the smile function of (6) for Bands S1, S2, and S3, respectively. We also see that the differences are less than $<\sim$0.4 nm. While most of the results for Band S1 show positive values [Fig. 12(b)], those for Bands S2 and S3 show negative values [Fig. 12(c) and (d)]. This means that the values of $\delta\lambda$ for Band S1 are larger than the results derived from the smile function, while those for Bands S2 and S3 are smaller than the results derived from the smile function, indicating a wavelength dependence of $\delta\lambda$.

From these results, we conclude that the difference in the smile function used to update the smile correction table is less than $\sim$0.4 nm for both VNIR and SWIR.

C. Evaluation of HISUI Data After the Update

Finally, we examined how the updated table reduces spectral smile in the HISUI data. Although the EA data have not yet been obtained since September 29, 2021, two NR mode datasets were downloaded to the ground using the ISS communication system. Both observation areas are relatively homogeneous, flat barren regions, where the method in this study can be used to evaluate spectral smile. One is a barren area near the Karakum Desert in Turkmenistan measured on October 2, 2021 (ID 211 002) and the other is a barren area near Tonalea in USA measured on October 25, 2021 (ID 211 025). Unfortunately, the Karakum Desert itself was not observed, only the areas close to it. Fig. 13 shows the positions

TABLE VII
COEFFICIENTS OF THE SMILE FUNCTION

	a_0	a_1	a_2
VNIR	-1.48 ± 0.15	$(5.36 \pm 0.72) \times 10^{-3}$	$(-5.47 \pm 0.69) \times 10^{-6}$
SWIR	-4.73 ± 0.04	$(9.59 \pm 0.21) \times 10^{-3}$	$(-1.20 \pm 0.02) \times 10^{-5}$

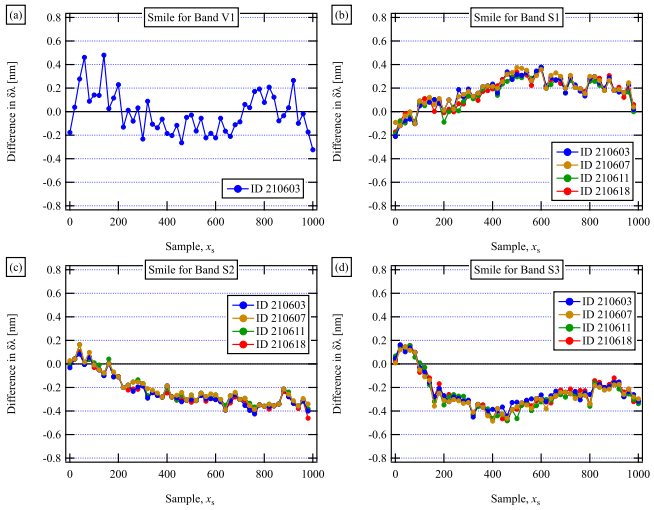

Fig. 12. (a) Difference in $\delta\lambda$ between the result in Fig. 7(a) and the smile function of (5) for Band V1. (b)–(d) Difference in $\delta\lambda$ between the result in Fig. 10(a)–(c) and the smile function of (6) for Bands (b) S1, (c) S2, and (d) S3, respectively.

to determine $\delta\lambda$ and W_{FM} (black '+' symbols) plotted on color composite images for the VNIR data of IDs 211 002 and 211 025.

In Fig. 14(a), the average of $\delta\lambda$ of the five lines for Band V1 is plotted against x_s, where the value of $\delta\lambda$ is offset so that $\delta\lambda = 0$ at $x_s = 0$ to make it easier to see how $\delta\lambda$ depends on x_s. It can be seen that $\delta\lambda$ shows a variation of approximately ± 0.2 nm but does not show a clear cross-track dependence. Indeed, quadratic curve fitting resulted in $\Delta\lambda_{\max} = 0.25$ nm both for IDs 211 002 and ID 211 025 [dotted lines in Fig. 14(a)]. This suggests that the updated table reduces the VNIR spectral smile to less than 0.25 nm. It is also seen that there is no significant difference in $\delta\lambda$ between IDs 211 002 and 211 025. In Fig. 14(b), W_{FM} for Band V1 is plotted against x_s, where we can see that the values of W_{FM} are almost constant between 13.5 and 14.0 nm. It is also seen that there is no significant difference between IDs 211 002 and 211 025. As mentioned in Section IV-B, because W_{FM} depends on the wavelength deviation of each pixel, appropriate correction of the spectral smile results in simultaneously correcting the cross-track dependence of W_{FM}. Thus, we can conclude that the updated table provides accurate correction for the spectral smile and cross-track dependence of W_{FM} in VNIR.

In Fig. 14(c), the average values of $\delta\lambda$ for Bands S1, S2, and S3 are plotted against x_s, where the value of $\delta\lambda$ is offset so that $\delta\lambda = 0$ at $x_s = 0$. Contrary to VNIR, it is clear that the spectral smile remains for all three bands. However, the maximum differences $\Delta\lambda_{\max}$ become smaller than those before the update in Fig. 8. Table VIII summarizes $\Delta\lambda_{\max}$

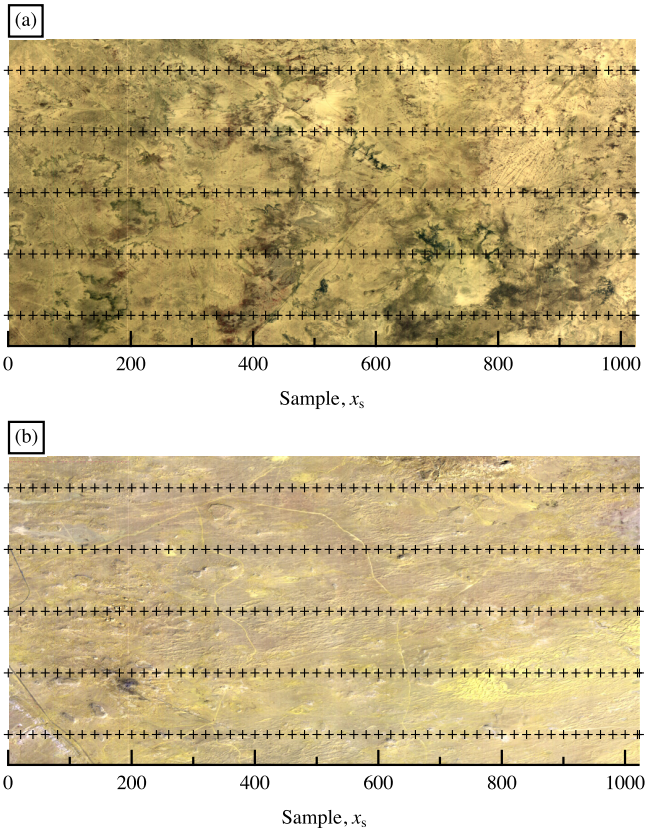

Fig. 13. (a) Color composite image for a barren area between the coast of the Caspian Sea and the Karakum Desert in Turkmenistan (ID 211 002), where red, green, and blue are assigned to the bands of 725, 515, and 665 nm, respectively. Black "+" symbols indicate the positions used to determine $\delta\lambda$ and W_{FM}, where $\delta\lambda$ and W_{FM} are obtained at 20-sample intervals in five different lines. (b) Color composite image observed for a barren area near Tonalea in USA (ID 211 025).

TABLE VIII
COMPARISON OF MAXIMUM VARIATION IN SPECTRAL SMILE BEFORE AND AFTER UPDATE OF THE SMILE CORRECTION TABLE

Before or after update	Band V1	Band S1	Band S2	Band S3
Before	1.8 nm	4.5 nm	4.4 nm	4.3 nm
After	< 0.25 nm	2.2 nm	2.2 nm	2.1 nm

before and after the update of the smile correction table, where we can see that $\Delta\lambda_{\max}$ after the update is almost half that before the update. We also found that there is no clear difference in $\delta\lambda$ between IDs 211 002 and 211 025 within $\delta\lambda \sim 0.2$ nm, indicating no significant scene-to-scene or short-term diurnal variations in the spectral smile. In Fig. 14(d), W_{FM} for Bands S1, S2, and S3 is plotted against x_s, where W_{FM} exhibits the cross-track dependence with maximum variations of 2.5–2.7 nm (Band S1), 2.5 nm (Band S2), and 3.2–3.3 nm

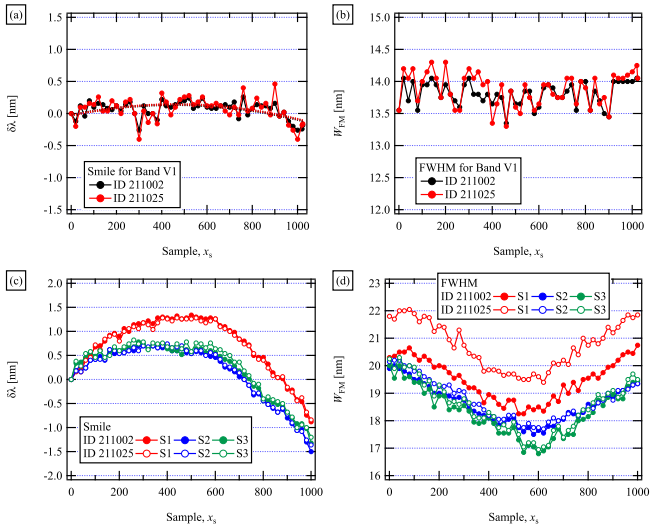

Fig. 14. (a) $\delta\lambda$ and (b) W_{FM} for Band V1 for IDs 211 002 and 211 025. The dotted lines in (a) indicate the results of quadratic curve fitting (black for ID 211 002 and red for ID 211 025). (c) $\delta\lambda$ and (d) W_{FM} for Bands S1, S2, and S3 for IDs 211 002 and 211 025. The values of $\delta\lambda$ in (a) and (c) are offset so that $\delta\lambda = 0$ at $x_{\mathrm{s}} = 0$.

(Band S3). While there is no clear difference in W_{FM} between IDs 211 002 and 211 025 for Bands S2 and S3, the difference for Band S1 is ∼1.5 nm. This difference may be attributed to the heterogeneity of the target surface and/or a local minimum for estimating an optimal value of W_{FM}. Nevertheless, it is important to note that despite the slight difference of W_{FM} between IDs 211 002 and 211 025, there is no clear difference in spectral smile for Band S1, as shown in Fig. 14(c).

The reason for spectral smile with $\Delta\lambda_{\max} = 2.1$–$2.2$ nm remaining in SWIR may be due to the wavelength dependence of the spectral smile. For example, as shown in Fig. 14(c), there are differences in the overall trend of $\delta\lambda$ among Bands S1, S2, and S3, indicating the wavelength dependence of the spectral smile. In contrast, Fig. 14(c) shows that the maximum difference in $\delta\lambda$ among Bands S1, S2, and S3 is <1.0 nm, which is less than $\Delta\lambda_{\max} = 2.1$–$2.2$ nm. Thus, the spectral smile with $\Delta\lambda_{\max} = 2.1$–$2.2$ nm may not be explained only by the wavelength dependence. Another possibility is that while the smile correction table assumes that the FWHM of a single pixel is constant, the FWHM of a single pixel in SWIR may not be completely uniform, resulting in the possibility that the determination of the smile correction table did not fully reflect the actual characteristics of the spectral smile. In this case, it is necessary to determine a smile correction table that accounts for the variation of FWHM in the cross-track direction, but this is a future issue.

In summary, the updated smile correction table improves the spectral smile and cross-track dependence of W_{FM} in VNIR and reduces the amount of spectral smile in SWIR to be within 2.1–2.2 nm. Note that these characteristics of the spectral smile are equivalent to the properties of the HISUI public data. In other words, for the HISUI public data observed after September 29, 2021, VNIR has a nearly flat spectral smile with <0.25 nm and SWIR has spectral smile characteristics within 2.1–2.2 nm. In contrast, for data prior to September 27, 2021, there are spectral smiles with about 1.8 nm in VNIR and with 4.3–4.5 nm in SWIR.

VI. Conclusion

This article reported on the initial analysis of the wavelength calibration of HISUI. We first checked the band allocation using atmospheric absorption bands in actual observation images. We found that the VNIR data are always shifted by one band (10 nm) to the shorter wavelength, which was considered to be due to a misallocation of the band center wavelengths in the HISUI binning process. In contrast, no band shift phenomenon was observed in SWIR, indicating that the band allocations were appropriate. The HISUI project has already corrected the band allocation for VNIR at the ground L0 process at the GDS and CDAS.

We then evaluated the spectral smile and FWHM of the HISUI SRF based on the atmospheric correction for actual observation images. We found that a significant spectral smile was observed in actual observation images, with the maximum variations of 1.8 nm in VNIR and 4.3–4.5 nm in SWIR. We also found a cross-track dependence of FWHM, in which the maximum variation of FWHM was ∼5.0 nm for VNIR and ∼2.5–3.5 nm for SWIR. The characteristics of the spectral smile found in this study are different from those using the onboard lamps, for which no obvious spectral smile has been reported so far. This difference can be attributed to the fact that the path of light from the onboard lamps is not exactly the same as the path of light through the full optical system of the HISUI instrument. We concluded that the smile correction table determined by the preflight test using the onboard lamps causes a "false spectral smile" in the actual observation images.

Based on the characteristics of the spectral smile, we then modeled and examined the smile functions used to update the smile correction table. Finally, we evaluated whether the updated table reduces the spectral smile in the HISUI data. For VNIR, we confirmed that there is a nearly flat spectral smile with <∼0.25 nm and FWHM is almost constant in the range from 13.5 to 14.0 nm. For SWIR, although the cross-track dependences are still present both in the spectral smile and FWHM, the updated table reduced SWIR spectral smile to <2.1–2.2 nm.

From the characteristics of the spectral smile presented in this article, we summarize the spectral properties of the HISUI public data as follows. For the HISUI public data obtained after September 29, 2021, VNIR has a nearly flat spectral smile with <∼0.25 nm, and SWIR has spectral smile characteristics within 2.1–2.2 nm. However, the data prior to September 27, 2021 contain spectral smiles with ∼1.8 nm in VNIR and 4.3–4.5 nm in SWIR.

Finally, we mention a mid- to long-term evaluation of spectral stability in the HISUI calibration plan. The original plan was to conduct a mid- to long-term evaluation of spectral stability using the onboard lamps, but this study revealed that it is necessary to evaluate the characteristics of the spectral smile using actual observation images for ground surfaces. However, since the ISS orbit is unstable and HISUI does not

have a pointing system, it is difficult to predict the timing of EA data acquisition. Thus, at this point, we cannot make any specific plans for mid- to long-term evaluation of spectral stability using actual observation images. In any case, we will continue to monitor the characteristics of the spectral smile using the atmospheric correction method for each acquisition of the EA data and will update the smile correction table as necessary.

ACKNOWLEDGMENT

The authors would like to thank T. Tachikawa and Y. Horiguchi for their cooperation in maintaining and providing the data. They would also like to thank the HISUI calibration WG members and those involved in the development of HISUI.

REFERENCES

[1] *HISUI*. Accessed: Jun. 27, 2022. [Online]. Available: https://www.jspacesystems.or.jp/en/project/observation/hisui/

[2] R. O. Green, "Spectral calibration requirement for Earth-looking imaging spectrometers in the solar-reflected spectrum," *Appl. Opt.*, vol. 37, no. 4, p. 683, Feb. 1998, doi: 10.1364/AO.37.000683.

[3] B.-C. Gao, M. J. Montes, C. O. Davis, and A. F. H. Goetz, "Atmospheric correction algorithms for hyperspectral remote sensing data of land and ocean," *Remote Sens. Environ.*, vol. 113, pp. S17–S24, Sep. 2009, doi: 10.1016/j.rse.2007.12.015.

[4] D. R. Thompson, B.-C. Gao, R. O. Green, D. A. Roberts, P. E. Dennison, and S. R. Lundeen, "Atmospheric correction for global mapping spectroscopy: ATREM advances for the HyspIRI preparatory campaign," *Remote Sens. Environ.*, vol. 167, pp. 64–77, Sep. 2015, doi: 10.1016/j.rse.2015.02.010.

[5] P. Mouroulis, R. O. Green, and T. G. Chrien, "Design of pushbroom imaging spectrometers for optimum recovery of spectroscopic and spatial information," *Appl. Opt.*, vol. 39, no. 13, p. 2210, May 2000, doi: 10.1364/AO.39.002210.

[6] N. Yokoya, N. Miyamura, and A. Iwasaki, "Preprocessing of hyperspectral imagery with consideration of smile and keystone properties," *Proc. SPIE*, vol. 7857, Nov. 2010, Art. no. 78570B, doi: 10.1117/12.870437.

[7] J. S. Pearlman, P. S. Barry, C. C. Segal, J. Shepanski, D. Beiso, and S. L. Carman, "Hyperion, a space-based imaging spectrometer," *IEEE Trans. Geosci. Remote Sens.*, vol. 41, no. 6, pp. 1160–1173, Jun. 2003, doi: 10.1109/TGRS.2003.815018.

[8] R. O. Green, B. E. Pavri, and T. G. Chrien, "On-orbit radiometric and spectral calibration characteristics of EO-1 hyperion derived with an underflight of AVIRIS and *in situ* measurements at Salar de Arizaro, Argentina," *IEEE Trans. Geosci. Remote Sens.*, vol. 41, no. 6, pp. 1194–1203, Jun. 2003, doi: 10.1109/TGRS.2003.813204.

[9] B.-C. Gao, M. J. Montes, and C. O. Davis, "Refinement of wavelength calibrations of hyperspectral imaging data using a spectrum-matching technique," *Remote Sens. Environ.*, vol. 90, no. 4, pp. 424–433, Apr. 2004, doi: 10.1016/j.rse.2003.09.002.

[10] A. Dadon, E. Ben-Dor, and A. Karnieli, "Use of derivative calculations and minimum noise fraction transform for detecting and correcting the spectral curvature effect (Smile) in hyperion images," *IEEE Trans. Geosci. Remote Sens.*, vol. 48, no. 6, pp. 2603–2612, Jun. 2010, doi: 10.1109/TGRS.2010.2040391.

[11] K. Staenz, R. A. Neville, S. Clavette, R. Landry, H. P. White, and R. Hitchcock, "Retrieval of surface reflectance from hyperion radiance data," in *Proc. IEEE Int. Geosci. Remote Sens. Symp.*, Jun. 2002, pp. 1419–1421, doi: 10.1109/IGARSS.2002.1026135.

[12] B. Datt, T. R. McVicar, T. G. Van Niel, D. L. B. Jupp, and J. S. Pearlman, "Preprocessing EO-1 hyperion hyperspectral data to support the application of agricultural indexes," *IEEE Trans. Geosci. Remote Sens.*, vol. 41, no. 6, pp. 1246–1259, Jun. 2003, doi: 10.1109/TGRS.2003.813206.

[13] B. Cairns, B. E. Carlson, R. Ying, A. A. Lacis, and V. Oinas, "Atmospheric correction and its application to an analysis of hyperion data," in *Proc. IEEE Int. Geosci. Remote Sens. Symp.*, vol. 41, Jun. 2003, pp. 1232–1244, doi: 10.1109/TGRS.2003.813134.

[14] L. Guanter, R. Richter, and J. Moreno, "Spectral calibration of hyperspectral imagery using atmospheric absorption features," *Appl. Opt.*, vol. 45, no. 10, p. 2360, Apr. 2006, doi: 10.1364/AO.45.002360.

[15] L. Guanter, V. Estellés, and J. Moreno, "Spectral calibration and atmospheric correction of ultra-fine spectral and spatial resolution remote sensing data. Application to CASI-1500 data," *Remote Sens. Environ.*, vol. 109, no. 1, pp. 54–65, Jul. 2007, doi: 10.1016/j.rse.2006.12.005.

[16] X. Ceamanos and S. Doute, "Spectral smile correction of CRISM/MRO hyperspectral images," *IEEE Trans. Geosci. Remote Sens.*, Nov. 2010, pp. 3951–3959, doi: 10.1109/TGRS.2010.2064326.

[17] K. Alonso *et al.*, "Data products, quality and validation of the DLR Earth sensing imaging spectrometer (DESIS)," *Sensors*, vol. 19, p. 4471, Oct. 2019, doi: 10.3390/s19204471.

[18] S. Cogliati *et al.*, "The PRISMA imaging spectroscopy mission: Overview and first performance analysis," *Remote Sens. Environ.*, vol. 262, Sep. 2021, Art. no. 112499, doi: 10.1016/j.rse.2021.112499.

[19] A. Iwasaki *et al.*, "Weighted binning of hyperspectral sensor: Application to hyperspectral imager suite (HISUI)," *Remote Sens.*, to be published.

[20] A. Iwasaki, J. Tanii, O. Kashimura, and Y. Ito, "Prelaunch status of hyperspectral imager suite (Hisui)," in *Proc. IEEE Int. Geosci. Remote Sens. Symp.*, Jul. 2019, pp. 5887–5890, doi: 10.1109/IGARSS.2019.8898660.

[21] M. Urai *et al.*, "Initial onboard calibration results of the HISUI hyperspectral sensor," in *Proc. IEEE Int. Geosci. Remote Sens. Symp. (IGARSS)*, Jul. 2021, pp. 1608–1610, doi: 10.1109/IGARSS47720.2021.9554224.

[22] M. Meroni *et al.*, "Characterization of fine resolution field spectrometers using solar Fraunhofer lines and atmospheric absorption features," *Appl. Opt.*, vol. 49, no. 15, p. 2858, May 2010, doi: 10.1364/AO.49.002858.

[23] R. Richter, D. Schlapfer, and A. Müller, "Operational atmospheric correction for imaging spectrometers accounting for the smile effect," *IEEE Trans. Geosci. Remote Sens.*, vol. 49, no. 5, pp. 1772–1780, May 2011, doi: 10.1109/TGRS.2010.2089799.

[24] J. Tanii, O. Kashimura, Y. Ito, and A. Iwasaki, "Flight model performances of HISUI hyperspectral sensor onboard ISS (international space station)," *Proc. SPIE*, vol. 10000, Oct. 2016, Art. no. 100000A, doi: 10.1117/12.2243846.

[25] K. K. Obata *et al.*, "An overview of ISS HISUI hyperspectral imager radiometric calibration," in *Proc. IEEE Int. Geosci. Remote Sens. Symp. (IGRASS)*, Jul. 2016, pp. 1924–1927, doi: 10.1109/IGARSS.2016.7729495.

[26] D. R. Thompson *et al.*, "Imaging spectrometer stray spectral response: In-flight characterization, correction, and validation," *Remote Sens. Environ.*, vol. 204, pp. 850–860, Jan. 2018, doi: 10.1016/j.rse.2017.09.015.

[27] S. Yamamoto, H. Mizuochi, M. Matsuoka, K. Iwao, and S. Tsuchida, "Analysis based on onboard lamp and lunar vicarious calibrations for sensitivity degradation of a hyperspectral sensor," *IEEE Trans. Geosci. Remote Sens.*, vol. 60, pp. 1–12, 2022, doi: 10.1109/TGRS.2021.3127163.

Satoru Yamamoto received the Ph.D. degree in science from Kobe University, Kobe, Japan, in 1999.

He is currently a Senior Researcher with the Research Institute of Geology and Geoinformation, Geological Survey of Japan, National Institute of Advanced Industrial Science and Technology, Tsukuba, Japan. He is involved in the Earth observation remote sensing projects of ASTER and HISUI and the Lunar Mission Project of SELENE/Kaguya.

Dr. Yamamoto is a member of the Japanese Society of Planetary Sciences, the Japan Geoscience Union, and the Remote Sensing Society of Japan.

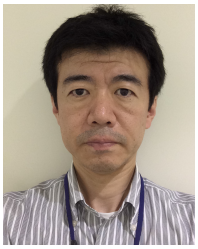

Satoshi Tsuchida received the B.S. degree in geology and the Ph.D. degree in mineral resources engineering from Waseda University, Tokyo, Japan, in 1986 and 1991, respectively.

In 1992, he joined the Geological Survey of Japan (GSJ), National Institute of Advanced Industrial Science and Technology, Tsukuba, Japan, to engage in research in geological and environmental remote sensing and calibration of radiometers on satellites, where he is currently a Principal Research Manager.

Minoru Urai received the Ph.D. degree in science from Kagoshima University, Kagoshima, Japan, in 2004.

He joined the Geological Survey of Japan, National Institute of Advanced Industrial Science and Technology, Tsukuba, Japan, where he is engaged in research on volcano observation using remote sensing in 1981. He moved to the National Institute of Advanced Industrial Science and Technology (AIST), into which the Geological Survey of Japan and 15 other national institutes were reorganized in 2001. He joined Japan Space Systems, Tokyo, Japan, in 2021. He has been a Collaborating Visitor of AIST since 2021.

Hiroki Mizuochi received the Ph.D. degree in environmental studies from the University of Tsukuba, Tsukuba, Japan, in 2017.

He is currently a Researcher with the Research Institute of Geology and Geoinformation, Geological Survey of Japan, National Institute of Advanced Industrial Science and Technology, Tsukuba. He is involved in the Earth observation remote-sensing projects of ASTER and HISUI, and Pan-Arctic Water-Carbon Cycles JSPS scientific research.

Dr. Mizuochi is a member of the Remote Sensing Society of Japan, the Japan Society of Photogrammetry and Remote Sensing, and the Japan Geoscience Union.

Koki Iwao received the Ph.D. degree (Doctor of Engineering) from The University of Tokyo, Tokyo, Japan, in 2000.

He is currently the Group Leader of the Remote-Sensing Research Group, Research Institute of Geology and Geoinformation, Geological Survey of Japan, National Institute of Advanced Industrial Science and Technology, Tsukuba, Japan. He is involved in the Earth observation remote-sensing projects of ASTER and HISUI.

Dr. Iwao is a member of the Remote Sensing Society of Japan, the Japan Society of Photogrammetry and Remote Sensing, and the Japan Association of Surveyors.

Akira Iwasaki received the M.Sc. degree in aerospace engineering and the Ph.D. degree in engineering from The University of Tokyo, Tokyo, Japan, in 1987 and 1996, respectively.

He joined the Electrotechnical Laboratory, The University of Tokyo, in 1987, where he engaged in research on space technology and remote sensing system. He is currently a Professor with The University of Tokyo. He is also the Project Leader of the Japanese hyperspectral sensor, Hyperspectral Imager Suite (HISUI) on the International Space Station.

Dr. Iwasaki received the 2015 Best Reviewers Award of the IEEE TRANSACTIONS OF GEOSCIENCE AND REMOTE SENSING in 2014. He was the General Chair of the 7th IEEE GRSS Workshop on Hyperspectral Image and Signal Processing Evolution in Remote Sensing (WHISPERS) in 2015 and the Technical Co-Chair of the International Geoscience and Remote Sensing Symposium 2019 (IGARSS 2019).